PR Adjusted TMI Estimation of Rainfall

Peter Bauer

European Centre for Medium-Range Weather Forecasts

Summary: A new methodology for the combination of active and passive microwave measurements for near–surface precipitation retrieval from TRMM data was developed in the framework of the EuroTRMM project. The approach consists of a stand–alone passive microwave algorithm which is calibrated by colocated radar estimates. The passive microwave technique was based on combined cloud model–radiative transfer simulations including varying surface conditions, a melting layer parameterization, and approximative three–dimensional radiative transfer modeling. The representativeness of the simulations with respect to TMI observations was evaluated replacing brightness temperatures (TBs) by empirical orthogonal functions (EOFs). Comparing the principal components to those from TMI observations containing precipitation revealed that the 85.5 GHz TBs from the simulations represent the major source of mismatch. This is due to the accumulation of uncertainties in cloud model parameterizations of ice microphysics and approximative radiative transfer at this frequency where scattering is most efficient.

Depending on the lowest detectable rainfall threshold, the available simulations covered 88–99% of observations obtained from colocated TMI–PR measurements. Gaps occurred mostly for less intense cloud systems which are not well represented by the cloud model simulations. The ambiguity of observations, i.e., the multiplicity of hydrometeor profiles with the same passive microwave signature was also analyzed. It was found that ambiguity decreases with increasing intensity of the observed scene. Excluding the 85.5 GHz channels clearly produced less ambiguity. About 80–95% of all cases showed less than 50% standard deviation of the retrieval variable per TB–vector compared to 65–85% when the 85.5 GHz channels were included.

The TMI retrieval technique employs a simplified Bayesian estimator applied to the simulations characterized by 2 EOFs representing either 7 or 9 TBs. Compared to PR estimates of near–surface rainfall integrated over the TMI field of view, the 7–channel algorithm performed consistently better than the 9–channel algorithm. This confirmed the previous analysis of database gaps as a function of lower rain detection threshold. Sensor combination is carried out by gridding PR estimates of rain liquid water content to the TMI observation geometry. A liquid water dependent database collects common samples over the narrow swath covered by both TMI and PR. Average calibration functions are calculated and dynamically updated along the satellite track and applied to the full TMI swath.

The behavior of the calibration function is relatively stable. The TMI estimates showed a significant underestimation of rainfall at low rain liquid water contents ($< 0.3\,gm^{-3}$) as well as at very high rainfall intensities ($> 1\,gm^{-3}$). Between these limits, the mismatch was less significant with a tendency towards overestimation. These biases were found to be neither raintype nor beam–filling dependent.

The standard deviations between instantaneous TMI and PR estimates after calibration may be interpreted as a total retrieval error assuming the PR estimates are unbiased. The error characteristics showed a rather constant absolute error of $< 0.05\,gm^{-3}$ for rain liquid water contents $< 0.2\,gm^{-3}$. Above, the error increases to $0.1\,gm^{-3}$ for amounts up to $1\,gm^{-3}$. In terms of relative errors, this corresponds to a sharp decrease from $>100\%$ to 25% between $0.01\,gm^{-3}$ and $0.2\,gm^{-3}$. The standard deviation of near–surface rain liquid water contents with the same radiometric signature provides a means to estimate the contribution from the simulations to this error. In the range where TBs respond most sensitively to rainwater contents, almost the entire error originates from the ambiguity of signatures. At very low and very high rainrates ($< 0.05\,gm^{-3}$ and $> 0.7\,gm^{-3}$) at least half of the total error is explained by the inversion process.

1 Introduction

Only microwave radiometers can provide a physically reasonable rainfall estimate with sufficient spatial coverage. However, radar estimates are considered more accurate due to less signal contribution from precipitating ice and non–precipitating hydrometeors together with a better spatial resolution.

Therefore, a combination of both passive and active measurements can take advantage of the accuracy of radar estimates and the spatial coverage and operational availability of radiometer observations.

The motivation of this work is manyfold, (1) the objective of developing a combined active–passive microwave rainfall retrieval technique which is computationally efficient to be applied globally in an operational manner, (2) to provide instantaneous estimates on a pixel–by–pixel basis for high–resolution validation and process studies, (3) to be able to quantify retrieval errors, (4) to prepare intercalibration between products from satellites of which only one carries a radar (e.g. the Global Precipitation Mission, GPM).

The Tropical Rainfall Measuring Mission (TRMM, Kummerow et al. 1998) microwave standard algorithms represent either single–sensor or multiple–sensor profile retrievals (data products 2A-12, 2B-31; Kummerow et al. 1996, Haddad et al. 1997) utilizing measurements from the TRMM Microwave Imager (TMI) and the Precipitation Radar (PR). The multiple–sensor technique (2B-31) involves a high computational effort and strong reliance on the PR–input because the PR reflectivity profiles serve as direct predictors along with TMI brightness temperatures. This approach suffers from the required viewing geometry and spatial resolution adjustment of the conically tracking TMI and the cross–tracking PR which produces large uncertainties given the large vertical and horizontal variability of hydrometeor profiles.

The methodology presented here focuses on the development of a stand–alone TMI algorithm which is dynamically calibrated by bulk parameters obtained from PR data. The lesser degree of dependence on the radar in the primary retrieval step requires a thorough preparation of the so–called training databases. These represent the set of hydrometeor profile–surface condition combinations which are supposed to be representative for the observed scenes and which are to be used for inversion by whatever method. The experience from physical algorithm development and evaluation efforts (e.g. Smith et al. 1998, Ebert and Manton 1998) suggests that the most sensitive point of algorithm performance is the forward modeled database rather than the inversion technique.

The approach therefore attempts to treat the major problems in the forward step with great care (radiative transfer, surface variability, bulk microphysics) because it is believed that the investigation of minor uncertainties without proper treatment of their major counterparts may lead to erroneous interpretation of real measurements. The largest uncertainty is introduced by the cloud model itself. The limited availability of cloud model simulations of this type already biases a possible database by the selection of model type and simulation experiments.

The idea of using the PR rainfall estimates as a calibration tool rather than as an input for the retrieval procedure itself has two major advantages. Firstly, the problem of different viewing geometries of TMI and PR is avoided. This would require either the accumulation of a three–dimensional data–space with PR profiles within the TMI effective field of view (EFOV) or a strong simplification of the match–up geometry. The latter would average out the spatially well defined information which is available from the PR in the first place. Secondly, usage of PR data as a retrieval variable restricts the application of the combined algorithm to the narrow swath where both data sources are available. Missing this information on the wide swath would produce algorithm instability compared to a simple rainrate dependent calibration. Again, a calibration of this kind may be easier transferred to other sensors once it is globally stable.

Calibrating TMI retrievals with PR estimates is based on the assumption that the PR estimates are unbiased. A by–product of the calibration is the estimation of the common uncertainty, that is the remaining random 'error'. This is a very important information, for example when these products are assimilated in forecast models (e.g. Marecal and Mahfouf 2000).

This paper is divided into two major parts, i.e., the description of the forward modeling problem

(Section 2) including an estimation of database representativeness and the set–up and evaluation of the TMI–only and TMI–PR combined algorithms (Section 3). Section 2 represents the contribution to WP–4200 and Section 3 that to WP–5100. More details on both forward modeling and retrieval methodology are given in Bauer (2001) and Bauer et al. (2001).

2 Database analysis

2.1 Radiative transfer

All sensor specific radiative transfer tools are designed for the TMI with five channels at 10.65, 19.35, 21.3, 37.0, and 85.5 GHz center frequencies which measure the upwelling microwave radiances at both vertical and horizontal polarizations, except the 21.3 GHz channel which only measures vertically polarized radiances. The model is easily transferrable to similar sensors such as the Special Sensor Microwave Imager (SSM/I) or the Advanced Microwave Scanning Radiometer (AMSR). The layout of the radiative transfer model is summarized in Bauer et al. (1998) and Bauer (2001).

TMI zenith angles considered are between 47 and 54 degrees. This variation is a consequence of the comparably low earth orbit of TRMM at ~350 km altitude which increases the influence of the earth's ellipsoidal shape on the observation geometry. Spatial resolutions of the TMI channels refer to the 3 dB halfwidths of idealized, Gaussian shaped gain functions. The employed effective fields of view (EFOV) are the result of the instantaneous fields of view integrated over sampling time. This results in EFOV–dimensions of 44 km x 27 km, 30.4 km x 19.9 km, 27.2 km x 18.3 km, 16.0 km x 12.6 km, and 7.2 km x 6.0 km for the above channels. The resolution of the 10.65 GHz channel is somewhat enhanced because a deconvolution technique (Bauer and Bennartz 1998) is applied in the retrieval step (see Section 3). As a consequence of the deconvolution, the dynamic range of brightness temperatures is considerably enhanced ensuring that sensor noise amplification remains acceptable.

Table 1: Cloud model simulations.

Model	Ex. Reference	Cloud System	Resolution	Time Steps
GCE/TC-1	Tao and Simpson (1993)	squall line, TOGA-COARE	1.0 km	120, 150, 180, 210 min.
GCE/TC-3	Tao and Simpson (1993)	squall line, TOGA-COARE	3.0 km	180, 240, 300, 360 min.
UW-NMS/HC-3	Tripoli (1992)	hurricane 'Gilbert'	3.3 km	3280, 3290, 3310 min.
JCMM/TC-1	Swann (1996)	squall line, TOGA-COARE	1.25 km	270, 360 min.
Méso-NH/TC-1	Redelsperger and Sommeria (1986)	squall line, TOGA-COARE	1.25 km	300, 360, 420, 480 min.

The employed hydrometeor distributions originate from various cloud models and their experiments to allow the intercomparison of database representativeness and definition of future modeling requirements. Since all models and various experiments have been described in literature (Olson et al. 1996, Panegrossi et al. 1998), no details are given other than the following short list as well as an overview including key references in Tab. 1:

- Goddard Cumulus Ensemble Model (GCE) initialized on conditions over the tropical west Pacific in the Tropical Ocean Global Atmosphere (TOGA) Coupled Ocean–Atmosphere Response

Experiment (COARE) Intensive Field Array (IFA) on February 22, 1993, with 1 km (GCE/TC–1), and 3 km (GCE/TC–3) grid resolutions. The simulations represent squall line–type cloud systems with a strong leading edge perpendicular to the background wind field.

- University of Wisconsin Non–Hydrostatic Modeling System which represents a tropical cyclone development over the Caribbean Sea at 3.3 km horizontal resolution (UW–NMS/HC–3) after initialization with soundings at Kingston, Jamaica, 36 hours before the passage of hurricane Gilbert in September 1988.

- Large eddy models of the Met Office (JCMM/TC–1) and Météo France (Méso–NH/TC–1) with 1.25 km resolutions initialized on the same conditions as GCE/TC.

To avoid unrealistic cases, only those model time steps were chosen which seemed to present cloud systems at a mature and decaying development stage. Earlier time steps often showed the characteristics of the initialization set–up. From the UW–NMS/HC–3 experiment, periods with the lowest ice concentrations were taken because most of the others showed extended areas with integrated columns of graupel and snow well above $30\ kg/m^2$.

2.2 Evaluation of simulations

A simple method to reduce redundant information contained in the TMI channels is the calculation of empirical orthogonal functions (EOFs). For this, the collection of TB–vectors in the databases is decomposed into independent vectors by calculation of the covariance matrix of differences between the TBs and their average values. Then:

$$\mathbf{EOF_s} = \mathbf{E_s TB_s} \qquad (1)$$

The subscript 's' refers to simulations and $\mathbf{E_s}$ denotes the eigenvector matrix. Thus $\mathbf{EOF_s}$ and $\mathbf{TB_s}$ contain n simulations for m channels while $\mathbf{E_s}$ has the dimension m x m. Generally, the first three EOFs represent more than 98% of the total variability, so that the following evaluation can be restricted to two or three eigenvectors and eigenvalues. The main advantage of using EOFs instead of TBs is an efficient access to retrieval database entries by reducing the dimension of the observation vector.

Database merging was carried out by constructing screening masks for each cloud model simulation using data from ~130 TRMM orbits in August 1998. PR rain liquid water estimates, w_{PR}, were averaged to the TMI reference resolution of 27 km x 44 km. Only those cases were taken where $w_{PR} > 0.01\,gm^{-3}$ which resulted in ~ $2.8 \cdot 10^6$ samples. The average w_{PR} between 2–4 km altitude was taken for convenience since it is provided with TRMM standard product 2A25. The observed TBs (TB_o) were mapped on the simulated databases using the eigenvectors from the simulations, $\mathbf{E_s}$, by applying (1):

$$\mathbf{EOF_o} = \mathbf{E_s TB_o} \qquad (2)$$

The $\mathbf{EOF_o}$ were compared to those from the simulations, $\mathbf{EOF_s}$, and a mask was constructed only containing data where $w[\mathbf{EOF_s} = \mathbf{EOF_o}] \neq 0$. Then, all databases were merged by only including those simulations for which an entry in the masks existed thus where a set of TBs from the simulations actually had been observed. Finally, the EOFs were again calculated for the merged database (DBase–All). The advantage of this approach is that the frequency distribution of TBs and EOFs from the observations is now represented in the merged database. This was not the case for the original databases whose frequency distributions depended on the set–up of the cloud model experiments and radiative transfer calculations. This procedure was carried out twice, i.e., using the lower 7 channels and all 9 channels of the TMI. Keeping in mind that the cloud model input and radiative transfer

model would reveal their weaknesses at higher frequencies where scattering is strongest, a reduction of the TB–vector dimension is beneficial.

2.3 Database representativeness

Fig. 1 summarizes the TB–EOF statistics of all simulations and the observations. The panels in Fig. 1a show maximum, minimum, and mean TBs for all TMI channels. For each EOF the fractional explained variance is given in percent. UW–NMS/HC–3, GCE/TC–3, and Meso–NH/TC–1 represent more intense systems than GCE/TC–1 and JCMM/TC–1, i.e., the dynamic range of TBs is larger. This is because 10.65 GHz TBs are higher due to more volume emission while 85.5 GHz TBs are lower as a result of more volume scattering. The observations contain as much variability as the more intense simulations. 85.5 GHz TBs as low as 100 K are present. Comparing the merged database with the observations shows that the minimum 21.3 GHz TBs are higher as a consequence of the high water vapor burden in the simulations. The range of 10.65 (v,h) and 19.35 GHz (v) TBs is very similar. The largest differences occur comparing 37.0 (v,h) and 19.35 GHz (h) minima. This indicates that even though surface variability was introduced the full scale of observable conditions can not be represented. Important is, however, that the mean values and the range between means and maxima compare well which represent the cloudy portion of the signal.

More insight is provided when EOFs are analyzed. Fig. 1b presents the eigenvectors of the first three EOFs when all 9 TMI channels are included while Fig. 1c shows the same for the first two EOFs when only the lower 7 channels are used. In the first case, roughly 97–98% of total variability is explained by the first three EOFs. The same holds for the first two EOFs when the 85.5 GHz channels are excluded. For less intense cloud systems, the first EOF represents cloud emission in the 9–channel database. With increasing precipitating water and ice contents, the first two EOFs depend on integrated water and ice paths with similar sensitivity. The more intense rain systems in UW–NMS/HC–3, GCE/TC–3, and Meso–NH/TC–1 show large positive values at low frequencies and large negative values at high frequencies in the eigenvector of the first EOF. Thus, the first EOF expresses a strong frequency and a moderate polarization dependence. It therefore represents the major response to rain liquid water with positive response (emission) at lower frequencies, balanced response (emission and scattering) at 37.0 GHz, and negative response (scattering) at 85.5 GHz. Generally, the observations show less scattering and emission thus represent weaker systems. At 37.0 GHz there is strong positive response but less negative sensitivity at 85.5 GHz.

The second EOFs of the 9–channel databases contain always positive eigenvectors. Weights increase with frequency but there is little to no polarization effect. This may be interpreted as a sensitivity to cloud ice above opaque raincloud layers. Lower frequencies (10.65, 19.35, 21.3 GHz) contribute little. Very obvious is the difference to observations where the signs are negative but the relative magnitudes are the same. This results from remaining scattering not captured by the first EOF where scattering was less represented than in the simulations. Important to notice is that after database merging, similar eigenvectors are obtained from both simulations and observations. This would not have been achieved by only concatenating the simulation databases.

In the 7–channel database, scattering features are generally reduced thus all eigenvector elements in the first EOF are positive. The EOF is polarization sensitive and all window channels (10.65, 19.35, 37.0 GHz) have almost similar weight. Magnitude and polarization difference of the eigenvector elements at 37.0 GHz indicate the representation of thinner clouds in the simulation. For example, GCE/TC–1 and JCMM/TC–1 show larger differences in 37.0 GHz polarization difference than the other simulations. The second EOF shows a similar picture than the first EOF of the 9–channel databases. Thus the interpretation is similar, i.e., a strong response to total rain liquid water path in more convective areas. Here, the influence of the merging process is less obvious; however, simulations

and observations show very similar patterns.

2.3.1 Database gaps

The management of databases by EOFs allows an efficient access to the entries and their comparison with observed radiances. Tab. 2 compiles the percentage of observations (used for the above described masking) for which an entry existed in the 9–channel and 7–channel databases, respectively. Several PR thresholds were chosen to assess database representativeness as a function of rain detection limit. The results illustrate a very different performance of each simulation with respect to observations. Those simulations representing weaker cloud systems (GCE/TC–1, JCMM/TC–1) perform worse than the others. The hurricane simulation also covers less observations. All databases reach their maximum coverage at a lower PR threshold of $\sim 1\,mm\,h^{-1}$. Thus less intense systems are not well represented for which database coverage ranges from 65–88%.

The merged database performs at least as well as the best individual simulation (Meso–NH/TC–1). However, it covers the observations less well for very low and very high rainfall intensities. At low intensities, the general increase of the (rainfall) signal–to–noise–ratio produces uncertain estimates. At higher intensities, contributions from higher frequency channels may deteriorate the representativeness. There, insufficiencies of cloud model ice parameterizations, the approximation of three–dimensional radiative transfer and the effects of ice particle size distributions accumulate their effects when scattering increases. However, over the middle range of lower rain cut–off values, 93–98% of the observations are contained in the database.

The 7–channel databases shows a somewhat different performance, i.e., worse results at low rainfall thresholds but better performances at high intensities. Thus loosing the 85.5 GHz information reduces the sensitivity to less intense systems but creates less vulnerability to the forward modeling errors as outlined above. The UW–NMS/HC–3 simulation shows much better behavior thus seems to contain problems in the ice phase (too much graupel). Again, Meso–NH/TC–1 performs very well. The merged database representativeness increases consistently with increasing threshold.

2.3.2 Database ambiguity

Database ambiguity is expressed by $\sigma(w)$ for each database entry. This is the standard deviation of w per **EOF**–vector, i.e., the standard deviation of the retrieval variable per observation/simulation. If the relationship between w and **TB** or **EOF** would be unique, $\sigma(w) = 0$.

Table 2: 9/7–channel database coverage (in %) as a function of w_{PR}/RR_{PR} (in gm^{-3}/mmh^{-1}) limit.

w/RR-limit	0.01/0.11	0.02/0.24	0.05/0.68	0.07/1.00	0.10/1.50	0.20/3.30
Samples	2,854,350	1,993,818	1,066,776	791,598	791,598	214,416
9–channels:						
UW-NMS/HC-3	71.5	79.7	88.5	90.5	91.5	90.4
GCE/TC-3	85.5	91.3	95.3	95.1	93.9	87.6
GCE/TC-1	75.9	85.2	91.2	90.8	88.4	76.2

Meso-NH/TC-1	88.3	93.8	97.9	98.2	98.1	97.2
JCMM/TC-1	65.1	73.7	73.6	68.6	60.5	41.2
Dbase-All	87.6	93.4	97.9	98.3	98.3	96.8
7-channels:						
UW-NMS/HC-3	77.1	86.5	95.8	97.5	98.1	98.3
GCE/TC-3	78.8	85.2	90.8	91.1	90.1	87.1
GCE/TC-1	66.6	77.3	88.5	90.2	90.1	84.6
Meso-NH/TC-1	76.7	85.5	95.4	97.4	98.1	98.2
JCMM/TC-1	65.3	76.4	88.6	90.1	89.7	83.2
Dbase-All	79.6	88.0	96.8	98.3	98.9	99.0

Fig. 2a shows the accumulative distribution of the relative ambiguity, $\sigma(w)/w$, for all simulations and the merged 7-channel database thus signal-to-noise-ratio. Principally, the merged database produces worse ambiguity than the worst simulation. In Fig. 2a, 80-95% of all simulations have $\sigma(w)/w < 50\%$. For the 9-channel database, 65-85% of all samples have $\sigma(w)/w < 50\%$ (Fig. 2b). Ambiguity decreases with w which indicates the improving signal-to-noise-ratio for precipitation with system intensity. Thus a retrieval can be expected to perform better for stronger rainfall. The remaining 10% with relative ambiguity > 100% in the 9-channel merged database are not present in the 7-channel database. Thus excluding the 85.5 GHz observations has the advantage of excellent database coverage and reduced database ambiguity except for very weak rainfall. Note also, that the curves in Figs. 2a and 2b may be interpreted as a measure for an upper accuracy limit achievable by a retrieval technique which was trained on the present databases.

3 Retrieval

3.1 Bayesian estimators

Both 2A12 and 2B31 TRMM standard algorithms rely on the Bayesian estimator which provides the most probable solution for a given TB-vector (including PR reflectivity profiles in the case of 2B31). The actual procedure requires an a-priori probability distribution of possible solutions as close as possible to real observations. Theoretically, this probability distribution is multivariate representing the correlation of all quantities (surface, atmosphere, observation conditions) as they occur in the atmosphere. The maximization of probability involves a minimization of a cost function giving a measure for the deviation of the actual guess from a previous estimate in parameter and observation space. This requires (1) a stable minimization technique which accounts for the possibility of multiple minima during the optimization and (2) the necessity of a forward operator providing simulations of observations using the actual state vector.

Evans et al. (1995) chose the clean but computationally more expensive way by creating a subset of a global a-priori database with TBs close to the observations followed by an optimization of the cost

function. Olson et al. (1996) and Kummerow et al. (1996) introduce the assumption that the global database itself represents the correct probability distribution of cloud profiles and surface conditions. Then, the optimization procedure reduces to an integration over the whole database giving weights to each simulation according to their distance from the i-th observations in TB–space:

$$E(\mathbf{P_i}) = \frac{\sum\limits_{i=1}^{n} \mathbf{P_i} \, exp[-0.5 \, J(\mathbf{P_i}))]}{\sum\limits_{i=1}^{n} exp[-0.5 \, J(\mathbf{P_i}))]} \tag{3}$$

with:

$$J(\mathbf{P_i}) = [\mathbf{TB}_o - \mathbf{TB}_s(\mathbf{P_i})]^T [\mathbf{O} + \mathbf{S}]^{-1} [\mathbf{TB}_o - \mathbf{TB}_s(\mathbf{P_i})] \tag{4}$$

$E(\mathbf{P})$ denotes the expected state vector, $\mathbf{TB_o}$ the observed TBs, the forward operator is $\mathbf{TB_s}$, and observation and simulation error covariance matrices are given by $\mathbf{O}$ and $\mathbf{S}$, respectively. Due to the lack of better knowledge, the latter are usually assumed to comprise only uncorrelated radiometric noise and no simulation errors (e.g. Olson et al. 1996).

Here, the approach of Kummerow et al. was used with some important modifications:

- As shown in Section 2, the cloud simulations do not represent the probability distribution required for the reduction of the minimization procedure per se. The intercomparison of EOFs from various models and simulations had shown that, in particular including the 85.5 GHz channels, large discrepancies occurred between all tested situations. As a consequence, a merged database was constructed from all cloud model simulations and 130 orbits of TMI data. This will represent more realistic situations without the bias in TB–distributions as introduced by single simulations.

- The cost function, $J(\mathbf{P_i})$, is calculated in EOF–space and not in TB–space. This reduces the dimension of the matrix operations from 9 or 7 to 2. As a consequence, the error covariance matrix is also transferred to EOF–space thus $(\mathbf{O} + \mathbf{S})^{-1}$ becomes $[\mathbf{E_s}(\mathbf{O} + \mathbf{S})\mathbf{E_s}^T]^{-1}$.

- The modeling errors are not assumed to be zero even though the forward operator itself may be technically very accurate. There is no general estimate of microwave radiative transfer errors in the presence of clouds; however, the uncertainty introduced by the additional surface variability model as well as numerous problems associated with e.g. particle shape and size spectra, multi-dimensional radiative transfer etc. will amount to errors other than zero. Thus we assumed errors of 2, 4, 4, 6, 10 K at 10.65, 19.35, 21.3, 37.0, 85.5 GHz. There was no correlation assumed between errors of different channels so that $(\mathbf{O} + \mathbf{S})$ is diagonal.

- Database integration is only carried out once for all possible EOF–combinations. This reduces the computational effort to a simple two–dimensional look–up table during application.

3.2 TMI–PR combination

TMI data is ingested as in the 1B11 standard product (calibrated and navigated TBs) on a grid according to the conical TMI–scan. TBs are recalibrated accounting for a bias not corrected for in products prior to V.5 (Schluessel, pers. communication). For enhancement of spatial resolution and TB dynamic range, a deconvolution technique is applied to the TBs at 10.65 GHz (Bauer and Bennartz 1998) making use of the strong overlap of adjacent EFOVs. This provides a resolution of 27 km x 44 km which rpresents the reference resolution for 104 EFOVs along the scan for all further

analyses ($= EFOV_{ref}$). The TMI–only retrievals described in the previous section provide the effective sensing altitude, z_{CG}, and the rain liquid water content, w_{TMI}, at that altitude and at $EFOV_{ref}$. The instantaneous retrieval of w_{PR} follows Ferreira et al. 2000). For a Gamma–type raindrop size dize distribution with shape parameter $\mu = 1$, as used in the simulations, a conversion to rainrate is possible with: $RR = 20.833\,w^{1.12}$ where $[RR] = mmh^{-1}$ and $[w] = gm^{-3}$. The error of this fit is well below 1% for $w \in [0, 2\,gm^{-3}]$.

A quantity like z_{CG} was chosen because it represents the altitude from which the bulk radiometric signal at a specific frequency originates (Bauer et al. 1998):

$$z_{CG} = \left[\int_{-z_T}^{z_T} C^*[T(z), \mu] dz \right]^{-1} \int_{-z_T}^{z_T} z C^*[T(z), \mu] dz \qquad (5)$$

with the normalized weighting function as introduced by Mugnai et al. (1993):

$$C^*[T(z), \mu] = \frac{k(z)}{\mu TB} J[T(z), \mu] exp \left[\int_z^{z_T} \frac{k(z)dz}{\mu} \right] \qquad (6)$$

where z_T and $-z_T$ denote the altitude of the top of the atmosphere of the upward and downward directed beams, respectively, while $J[T(z)]$ is the radiation source function at level z with temperature T and the cosine of the observation zenith angle $\mu = cos\theta$. $k(z)$ denotes the local extinction coefficient. z_{CG} thus provides a pointer to the altitude to which the measurement at this frequency is most sive. Consequently, a retrieval would provide the best estimate of a microphysical quantity at that altitude. With increasing atmospheric opacity, z_{CG} will increase and vice versa. At the resolution of the 10.65 GHz channel, z_{CG} is in the range of 0.0 to 1.5 km which is sufficiently low for $w(z_{CG})$ to be equivalent to near–surface precipitation.

Since the coordinates of the w_{PR}–profiles are determined by the PR scan geometry at $\mathbf{x}_{PR} = (x, y, z)_{PR}$, a gridding on the TMI–reference system at coordinates $\mathbf{x}_{TMI} = (x, y, z_{CG})_{TMI}$ has to be carried out:

$$w_{PR}(\mathbf{x}_{TMI}) = \frac{\int\limits_{EFOV_{ref}} \int\limits_{z_{CG}-\sigma(z_{CG})}^{z_{CG}+\sigma(z_{CG})} w_{PR}(\mathbf{x}_{PR}) G_{TMI}(x, y)_{PR} d\mathbf{x}_{PR}}{2\sigma(z_{CG}) \int\limits_{EFOV_{ref}} G_{TMI}(x, y)_{PR} dx_{PR} dy_{PR}} \qquad (7)$$

This includes:

1. The convolution with the antenna gain function, G_{TMI}, over $EFOV_{ref}$ which is approximated by a Gaussian shaped function with 3 dB–half widths of 27 km in cross–track direction and 44 km in along–track direction.

2. The averaging over altitude due to the uncertainty in the estimation of z_{CG} expressed by the retrieval standard error, $\sigma(z_{CG})$.

3. A threshold of 80% for the coverage of the TMI $EFOV_{ref}$ with valid PR estimates (having the classification 'rain certain' or 'no rain' from the 2A25 rain flag terminology) to avoid errors introduced by insufficient PR samples for calculating (7).

This procedure minimizes the effects of colocation problems due to the different observation geometries of both sensors. Firstly, the retrieval of single level values instead of profiles avoids the effort of matching beams which can only be achieved by increasing the volume considerably thus loosing profile information again. For example, assuming a pixel size of 45 km and a zenith angle of 52° would

require radar profiles over a distance of 85 km if the reflected atmospheric contribution is accounted for. Secondly, the variation of w_{PR} over $EFOV_{ref}$ provides an estimate of the expected accuracy once w_{PR} and w_{TMI} are compared. The estimation of surface rain liquid water content (or rainrate) may seem to be independent of reference altitude variations; however, passive microwave measurements provide volume rather than level information so that rain profile variations contribute to the evaluation of the spatial average at one level.

The 2A12 product was treated in a similar fashion as the PR data. The original estimates comprise surface rainfall rates and hydrometeor concentrations at predefined levels which were gridded to the spatial sampling on the 85.5 GHz pixel locations. As in (7), the actually retrieved z_{CG} was used to select the profile level followed by a spatial integration of w_{2A12} at this altitude over $EFOV_{ref}$. With this procedure, all products to be compared refer to the same altitude and resolution.

During the following step, the estimates of w from both TMI and PR algorithms are compared as a function of w. Due to the quasi–logarithmic probability distribution of w, the range of $log_{10}(w)$ was divided into intervals with indices:

$$i_w = \begin{cases} 10\,log_{10}(w) & : w \leq 0.5 gm^{-3} \\ 26\,w - 16 & : w > 0.5 gm^{-3} \end{cases} \tag{8}$$

so that $i_w \in [-20, 10]$ for $w \in [0.01, 1]gm^{-3}$. The switch to a linear relationship in (8) ensures a better resolution of the dynamic range at higher w.

Ratios of w_{PR} over w_{TMI} are collected in the intervals with a dynamic adjustment along the satellite track:

$$c(i_w) = n(i_w)^{-1} \sum_{n(i_w)} \frac{w_{PR}(\mathbf{x}_{TMI})}{w_{TMI}(\mathbf{x}_{TMI})} \tag{9}$$

Here, a number of 10 samples per interval is accumulated and an average ratio is calculated after each new entry. If more than ten data pairs are contained, the oldest is deleted and the most recent is included. A number of 10 has been chosen to find a compromise between stability and flexibility. Tests with larger numbers did not give substantially different results. Finally, all TMI samples over the swath are corrected by:

$$w^c_{TMI}(\mathbf{x}_{TMI}) = c(i_w)w_{TMI}(\mathbf{x}_{TMI}) \tag{10}$$

Since only the inner part of the TMI–swath is covered by PR samples, an application of the calibration to the total swath assumes a certain spatial and temporal constancy.

4 Results

Figs. 3, 4, and 5 show examples of 7–channel Bayesian retrievals before and after calibration, the corresponding w_{PR} distribution and 2A12 estimates. One obvious feature is the greater degree of detail in our results. The deconvolution technique increases the spatial resolution of the 10.65 GHz channel and the large number of profiles contained in the EOF database reproduces the dynamic range of rainfall very well. 2A12 shows less spatial definition since it contains less profiles and combines radiometric and spatial information which are always integrated over the full database.

The calibration has the effect of increasing lower w and decreasing higher w. Very high w are again increased; however, the few available samples for $w > 1\,gm^{-3}$ are difficult to interpret. For the squall–line off the East African coast (Fig. 4), only small differences between TMI and PR estimates are observed. The dynamic range of w is smaller than for cyclone 'Anacelle' (Fig. 3). The frontal system

off the North American east coast (Fig. 5) shows a slight positive bias of the TMI estimate. Both primary TMI retrievals (ours and 2A12) show similar gross features whose structure and dynamic range correspond well with w_{PR}.

Fig. 6a presents the average calibration curve that is the average ratio of w_{PR} and w_{TMI} from 12 orbits, i.e., $\sim$ 14,000 samples. The same ratios are shown for the calibrated data. The calibration compensates for underestimations for $w < 0.3\,gm^{-3}$ and for overestimation between 0.3 and 0.9 gm^{-3}. Above, there is less data available to derive conclusions. The statistics (not shown here) did not indicate a significant algorithm bias. The distribution of the biases per w–interval together with the frequency distribution of w obviously compensate each other. Thus, general statistics may be misleading. The more detailed analysis in Bauer et al. (2001) provided further insight for the interpretation: For all cloudtypes, the gradient of the calibration factor has a similar shape which suggests that the beam-filling is well covered in the simulations on which the algorithm was trained. It was evident, that the TMI–PR bias does only depend on w. Thus beam–filling and cloudtype dependent retrievals (as included in the PR w–Z relations) can not explain the rather consistent shape of the calibration curve.

Fig. 6b presents remaining standard deviations between calibrated TMI and PR estimates. They remain comparably constant at 0.05 gm^{-3} between 0.01 and 0.3 gm^{-3}. In terms of relative errors, we obtained 100% at $w = 0.05\,gm^{-3} \approx 0.5\,mm/h$, 50% at $w = 0.1\,gm^{-3} \approx 1.3\,mm/h$, and 25% at $w = 0.3\,gm^{-3} \approx 4.9\,mm/h$. These standard deviations do not contain errors from the PR retrievals. Assuming a 1 dBZ calibration accuracy, PR retrieval uncertainties are of the order of 15% which have to be taken into account when total errors are calculated.

It is interesting to notice that the ambiguity of the database, i.e., the standard deviation of w for similar EOFs is envelopped by the TMI–PR error curve. A possible interpretation is that it represents the relative contribution to the total retrieval error. This contribution would increase from low to moderate rain intensities and decrease again for high intensities. Between 0.2 and 0.6 gm^{-3}, i.e., 3 and 12 mm/h, the entire retrieval error would be due to signal ambiguity. This would also suggest that the error of the inversion is small in this range. Generally spoken, the contribution from the surface decreases with increasing atmospheric opacity. On the other hand, sensitivity to liquid precipitation decreases once noise from microwave scattering at precipitating ice particles increases and brightness temperatures saturate while polarization ratios approach zero. This, in fact, would suggest that the pure inversion error is lower in the middle range. However, the large ambiguity of different situations with the same gross emission and scattering features reaches a maximum so that the overall error remains constant. Thus Fig. 6b may be interpreted as a basic quantification of database vs. inversion error as a function of rain intensity.

5   Summary and Discussion

Based on available cloud model simulation experiments of tropical precipitating systems, the attempt of an evaluation of cloud model–radiative transfer representativeness was carried out for the purpose of feeding physical rainfall retrieval techniques based on passive microwave measurements. Five cloud model experiments from four models were collected, covering tropical squall lines and cyclones. The hydrometeor distributions were fed into an Eddington–type radiative transfer model which accounts for first–order three–dimensional effects. Various configurations of observation geometries and surface conditions were applied and a melting layer was included. Brightness temperatures were calculated at the microwave frequencies and both polarizations of the TMI applying idealized antenna patterns.

EOFs were found to provide a better indication of database representativeness than TBs due to their independence and due to the fact that 2–3 EOFs explain already $\sim$98% of the total variability. Main

differences between simulations and TMI observations occurred when 85.5 GHz channels were included in the analysis (9–channel database). This points at the largest error sources which are: (1) insufficient ice parameterizations in cloud models, (2) least accurate results from approximative radiative transfer model, (3) strongest influence of three–dimensional radiative transfer effects not covered by the model. In case only frequencies between 10.65 and 37.0 GHz were used (7–channel database), the individual databases showed better agreement with each other and with observations.

The databases from all model simulations were merged using TRMM observations. These were mapped onto a two–dimensional table by use of the eigenvectors obtained from the EOF–analysis. The same procedure was carried out for PR rainfall measurements after convolution to the spatial resolution of the TMI. Once the 85.5 GHz channels were excluded, the merged database showed a better overlap with the observations only counting observations with near–surface rain liquid water contents above $0.07\,gm^{-3}$. Below, the 85.5 GHz channels contribute important information. In any case, both 7–channel and 9–channel databases cover between 88% and 99% of the observations. Gaps occur mostly at low rainfall rates; however, the 9–channel database shows an increasing number of gaps once more intense rainfall occurs.

Another issue was the estimation of the non–uniqueness of the TB–cloud profile relationships which is one of the major retrieval error sources. Here, the 7–channel database clearly produces less ambiguity thus better signal to noise ratios than the 9–channel database. About 80–95% of all simulations have a standard deviation of the retrieval variable below 50% which reduces to 65–85% for the 9–channel database. This uncertainty decreases with system intensity. These magnitudes have to be considered when total errors of rainfall retrievals are estimated. This also leeds to the requirement that information other than the TB-vector at the actual location may help to narrow down the uncertainty, e.g., by criteria using spatial variability for stratiform–convective separation (e.g. Hong et al. 1999).

An approach for a combined TMI-PR retrieval technique was presented to obtain rain liquid water contents at levels close to the surface. This technique is based on a primary estimation of water contents from passive microwave radiometer observations. Both radar reflectivities and brightness temperatures are more sensitive to rain water content than rainrate because of their independence of particle fallspeeds. In all cases, water contents were retrieved at the center of gravity of the TMI 10.65 GHz weighting function. This represents the altitude from which the channel, which is most sensitive to rain, receives a maximum contribution. All products were convolved with an idealized 10.65 GHz TMI antenna pattern to a resolution of 27 km x 44 km. This procedure avoids all problems of beam adjustment due to the different scanning geometry and spatial resolution of both sensors. For profile retrievals, these can only be overcome by increasing the investigated volume considerably averaging out large information contents.

Dynamically adjusted calibration coefficients are determined which correct the TMI estimate. The calibration coefficients are a function of rainwater content itself to account for non–uniformities over the dynamic range. It is assumed that the calibration curve is a slowly varying parameter so that it can be applied over the full TMI swath after adjustment over the common part. This allows the full usage of the TMI swath with a constantly updated quality control by the PR. Analysis of the calibration curve shows that for $w > 0.1\,g\,m^{-3}$ the calibration is rather weak and comparably constant while for smaller contents spatial variability and lower sensitivity boundaries of both sensors cause significant differences. The TMI retrieval produced consistently lower estimates at low rainrates while a less pronounced overestimation at moderate rainrates was found. This behavior was independent of beam–filling and cloud type thus purely dependent on rainrate. At this point, there is no finite conclusion possbile.

However, the technique performed very well against TMI standard product 2A12 without relying on similar constraints such as stratiform–convective separation or geometric distance to convection. Our

technique also provides more spatial details since the reference resolution is better than that of the nominal 10.65 GHz EFOV.

A by-product of the algorithm is the calculation of the remaining standard deviation between TMI and TMI-PR estimates once the bias was removed. These may be considered as an instantaneous retrieval error estimate. It was found to be fairly constant at $0.05\,g\,m^{-3}$ for low to moderate rainrates. Thus relative error decreases from above 100% to below 25% as a function of w. The database ambiguity - which was estimated in part I of this study - seems to explain a large fraction of the total retrieval error at moderate to high rainrates. At 3-12 mm/h the error of the inversion would therefore be small due to the strongest gradient of the TB-w response curve in that range.

It is obvious, that the quality of the combined TMI-PR product is driven by the PR since it represents the calibration data source. Thus any change in PR standard products used as input data will change this reference. However, the TMI-only algorithm provides retrievals in any case and can be operated independently. Computational efficiency of the TMI-only technique is very high because only a two-dimensional look-up table is used. The most time-consuming factor during application is the convolution of the PR estimates to the TMI reference resolution, if a swath-by-swath calibration is desired. This could be simplified by a globally valid calibration. This is subject of further studies towards the development of inter-satellite calibration for GPM.

6 Acknowledgments

7 References

Bauer, P., and R. Bennartz, 1998: TMI imaging capabilities for the observation of rainclouds. Rad. Sci., **33**, 335-349.

Bauer, P., L. Schanz, and L. Roberti, 1998: Correction of three-dimensional effects for passive microwave retrievals of convective clouds. J. Appl. Meteor., **37**, 1619-1632.

Bauer, P., 2001: Over-ocean rainfall retrieval from multi-sensor data of the Tropical Rainfall Measuring Mission (TRMM). Part I: Design and evaluation of inversion databases. J. Ocean. Atmos. Tech., accepted.

Bauer, P., P. Amayenc, C. Kummerow, and E. Smith, 2001: Over-ocean rainfall retrieval from multi-sensor data of the Tropical Rainfall Measuring Mission (TRMM). Part II: Algorithm implementation. J. Ocean. Atmos. Tech., revised.

Ebert, E. and M. Manton, 1998: Performance of satellite rainfall estimation algorithms during TOGA-COARE. J. Atmos. Sci., **55**, 1537-1557.

Evans, F., J. Turk, T. Wong, and G. Stephens, 1995: A Bayesian approach to microwave precipitation retrieval. J. Appl. Meteor., **34**, 260-279.

Ferreira, F., P. Amayenc, S. Oury, and J. Testud, 2000: Study and test of improved rain estimates

from the TRMM precipitation radar. J. Appl. Meteor. (TRMM special issue), submitted.

Haddad, Z., E. Smith, C. Kummerow, T. Iguchi, M. Farrar, S. Durden, M. Alves, and W. Olson, 1997: The TRMM 'day-1' radar/radiometer combined rain-profiling algorithm. J. Meteor. Soc. Japan, **75**, 799-808.

Hong, Y., C. Kummerow, and W. Olson, 1999: Separation of convective and stratiform precipitation using microwave brightness temperatures. J. Appl. Meteor., **38**, 1195-1213.

Kummerow, C., W. Olson, and L. Giglio, 1996: A simplified scheme for obtaining precipitation and vertical hydrometeor profiles from passive microwave sensors. IEEE Trans. Geosci. Remote Sens., **34**, 1213-1232.

Kummerow, C., W. Barnes, T. Kozu, J. Shiue, and J. Simpson, 1998: The Tropical Rainfall Measuring Mission (TRMM) sensor package. J. Atmos. Ocean. Tech., **15** , 809-817.

Marécal, V. and J.-F. Mahfouf, 2000: Variational retrieval of temperature and humidity profiles from TRMM precipitation data. Month. Wea. Rev., **128**, 3853-3866.

Mugnai, A., E. Smith, and G. Tripoli, 1993: Foundations for statistical-physical precipitation retrieval from passive microwave measurements. Part II: Emission-source and generalized weighting function properties of a time dependent cloud-radiation model. J. Appl. Meteor., **32**, 17-39.

Olson, W., C. Kummerow, G. Heymsfield, and L. Giglio, 1996: A method for combined passive-active microwave retrievals of cloud and precipitation profiles. J. Appl. Meteor., **35**, 1763-1789.

Panegrossi, G. and co-authors, 1998: Use of cloud model microphysics for passive microwave-based precipitation retrieval: Significance of consistency between model and measurement manifolds. J. Atmos. Sci., **55**, 1644-1673.

Redelsperger, J.-L. and G. Sommeria, 1986: Three-dimensional simulation of a convective storm: Sensitivity studies on subgrid parameterization and spatial resolution. J. Atmos. Sci., **43**, 2619-2635.

Smith, E. and co-authors, 1998: Results of WetNet PIP-2 project. J. Atmos. Sci., **55**, 1483-1536.

Swann, H., 1998: Sensitivity to the representation of precipitating ice in CRM simulations of deep convection. Atmos. Res., **48**, 415-435.

Tao, W.-K., and J. Simpson, 1993: The Goddard cumulus ensemble model. Part I: Model description. Terr. Atmos. Ocean Sci., **4**, 35-72.

Tripoli, G., 1992: A non-hydrostatic model designed to simulate scale interaction. Mon. Wea. Rev., **120**, 1342-1359.
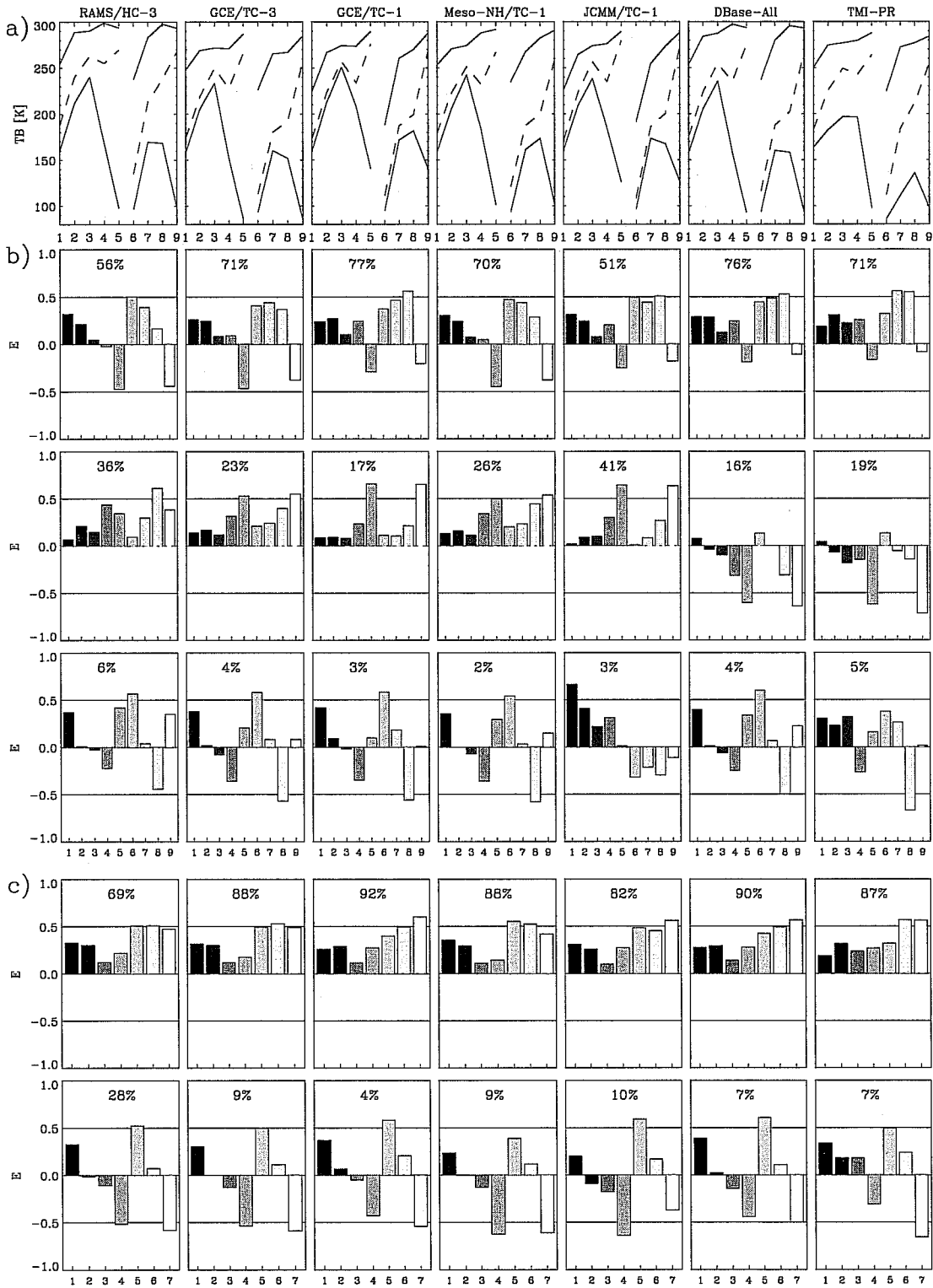
Figure 1: *Minimum, maximum (solid), and average (dashed) TBs from individual/merged simulations and TMI-PR observations (a). Channel numbers 1-9 refer to 10.65v, 19.35v, 21.3v, 37.0v, 85.5v, 10.65h, 19.35h, 37.0h, 85.5h. Figs. (b) give eigenvectors of first three 9-channel EOFs as well as percentiles of explained variance. Figs. (c) show corresponding eigenvectors for seven channel EOFs with channel numbers 1-7 referring to 10.65v, 19.35v, 21.3v, 37.0v, 10.65h, 19.35h, 37.0h.*
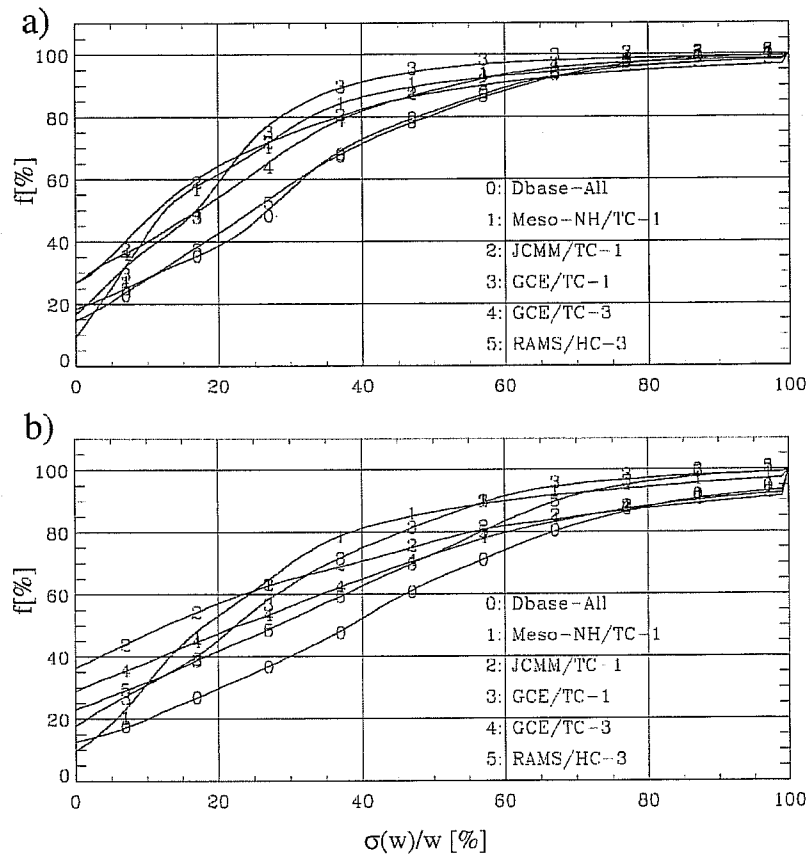
Figure 2: *Accumulated frequency distribution of relative variability in w from all simulations in the 7-channel database (a) and 9-channel database (b).*
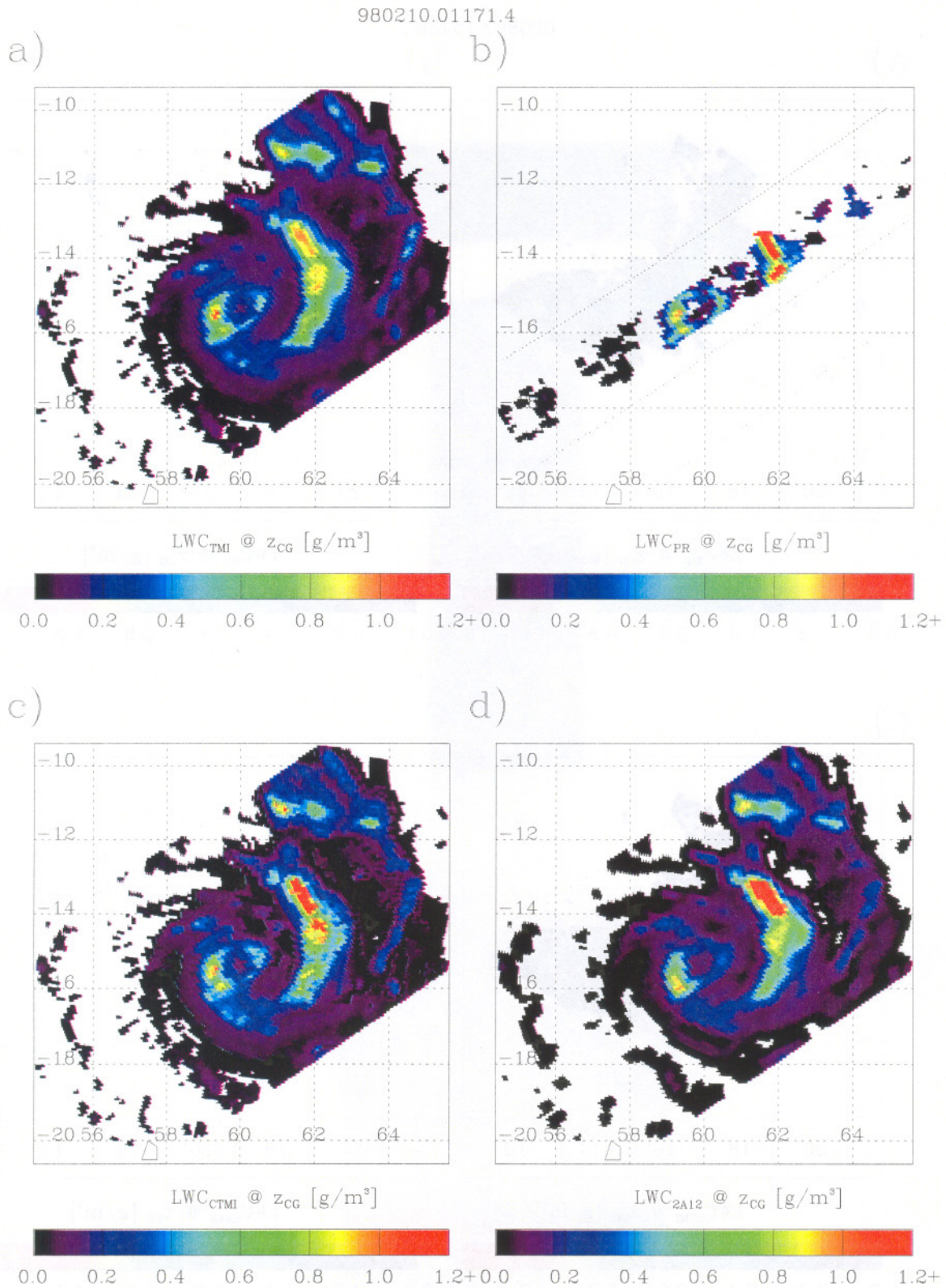
980210.01171.4

a)

LWC$_{TMI}$ @ z$_{CG}$ [g/m^3]

0.0   0.2   0.4   0.6   0.8   1.0   1.2+

b)

LWC$_{PR}$ @ z$_{CG}$ [g/m^3]

0.0   0.2   0.4   0.6   0.8   1.0   1.2+

c)

LWC$_{CTMI}$ @ z$_{CG}$ [g/m^3]

0.0   0.2   0.4   0.6   0.8   1.0   1.2+

d)

LWC$_{2A12}$ @ z$_{CG}$ [g/m^3]

0.0   0.2   0.4   0.6   0.8   1.0   1.2+

Figure 3: *Distributions of retrieved w from TMI–only 7–channel algorithm (a), PR estimates averaged to TMI reference resolution (b), calibrated w (c), and 2A12 V.5 algorithm; case: 980210.01171.*
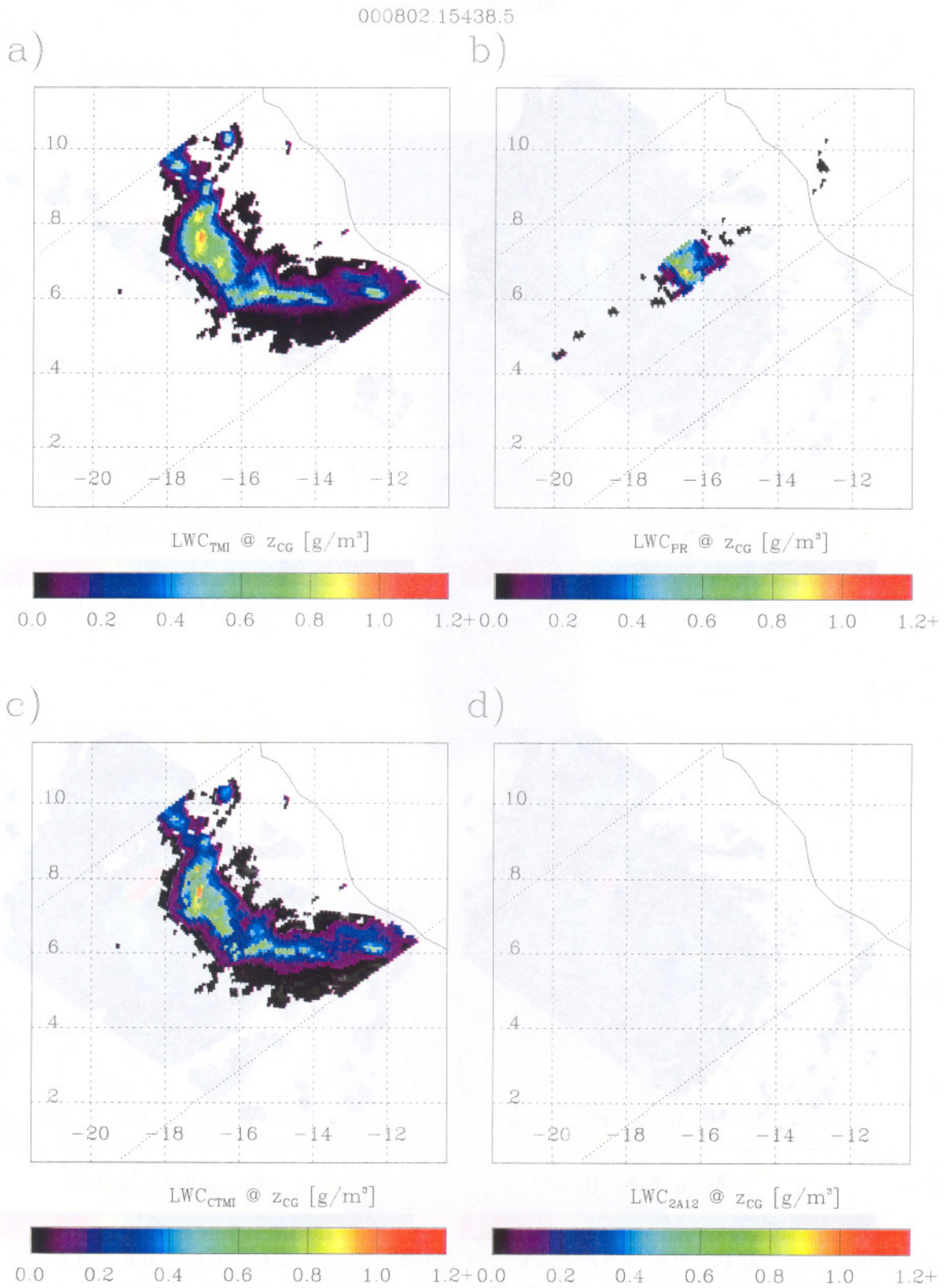
000802.15438.5

a)

b)

LWC$_{TMI}$ @ z$_{CG}$ [g/m³]

LWC$_{PR}$ @ z$_{CG}$ [g/m³]

0.0   0.2   0.4   0.6   0.8   1.0   1.2+   0.0   0.2   0.4   0.6   0.8   1.0   1.2+

c)

d)

LWC$_{CTMI}$ @ z$_{CG}$ [g/m³]

LWC$_{2A12}$ @ z$_{CG}$ [g/m³]

0.0   0.2   0.4   0.6   0.8   1.0   1.2+   0.0   0.2   0.4   0.6   0.8   1.0   1.2+

Figure 4: *As in Fig. 3 for case: 000802.15438 (no 2A12 product available).*

320

000830.15876.5

a)

LWC$_{TMI}$ @ z$_{CG}$ [g/m³]

0.0   0.2   0.4   0.6   0.8   1.0   1.2+

b)

LWC$_{PR}$ @ z$_{CG}$ [g/m³]

0.0   0.2   0.4   0.6   0.8   1.0   1.2+

c)

LWC$_{CTMI}$ @ z$_{CG}$ [g/m³]

0.0   0.2   0.4   0.6   0.8   1.0   1.2+

d)

LWC$_{2A12}$ @ z$_{CG}$ [g/m³]

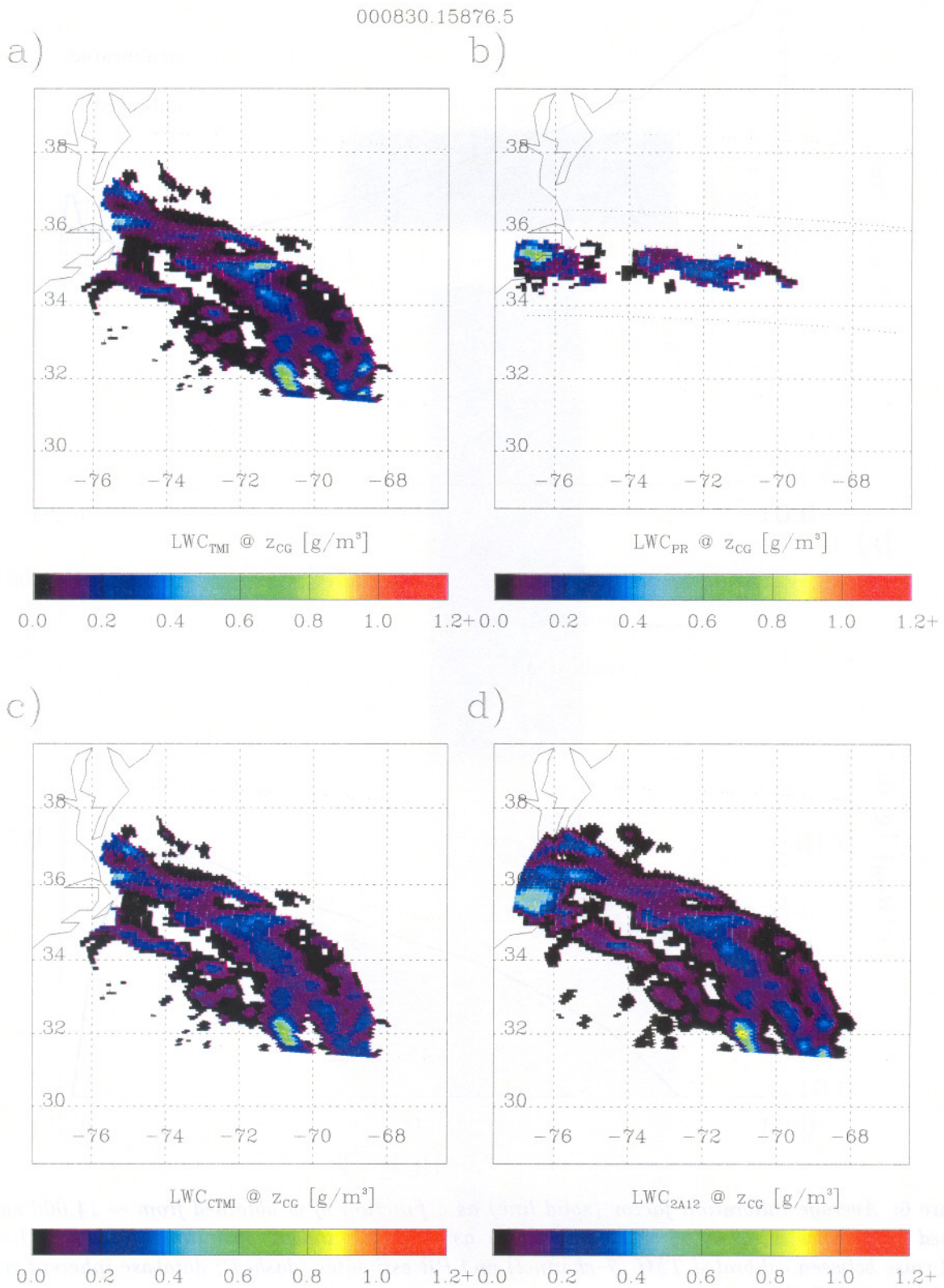0.0   0.2   0.4   0.6   0.8   1.0   1.2+

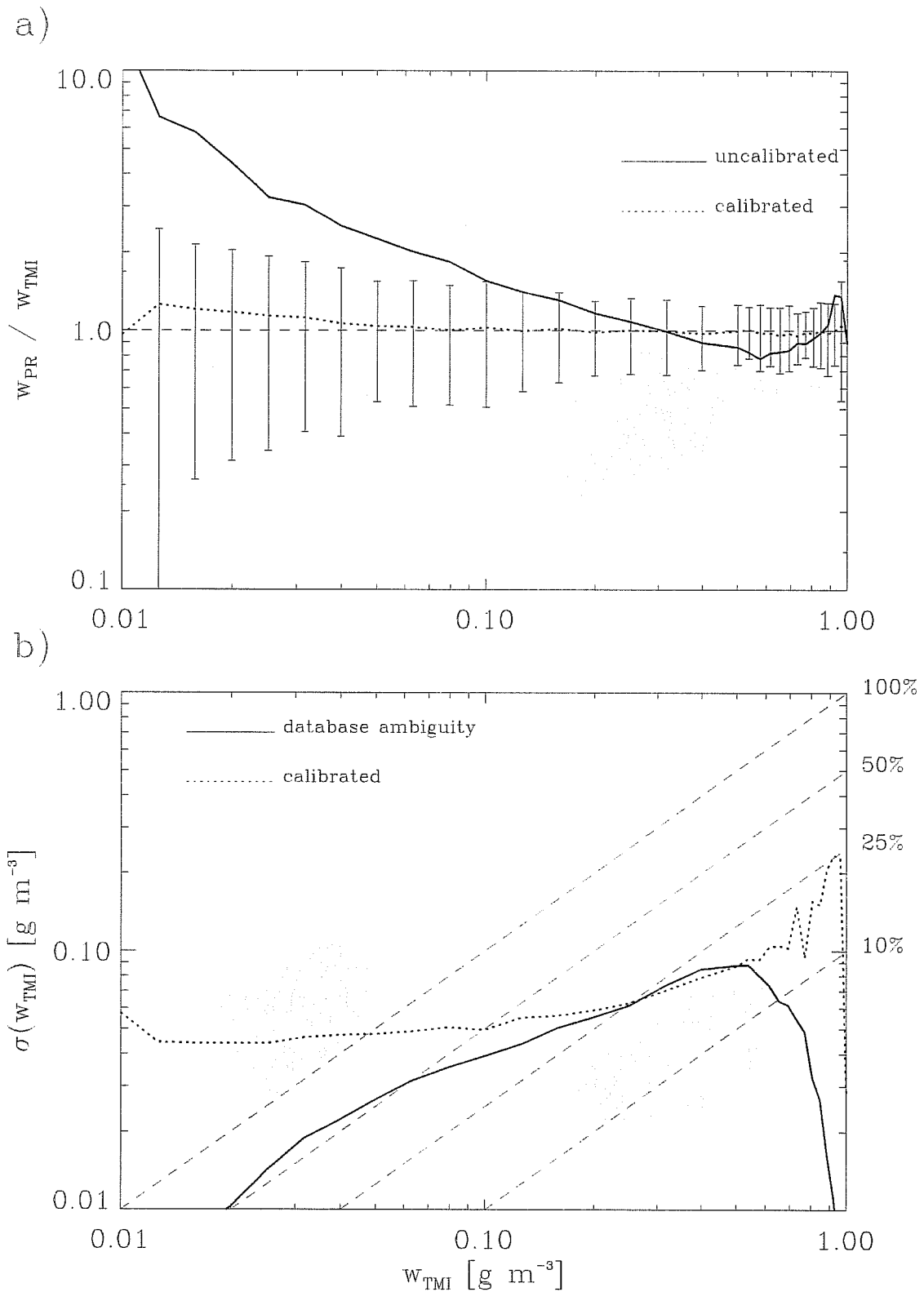Figure 5: *As in Fig. 3 for case: 000830.15876.*

a)

b)

Figure 6: *Average calibration factor (solid line) as a function of w obtained from $\sim$ 14,000 samples; dashed line shows w_{PR}/w_{TMI} after calibration as well as standard deviation of ratios (a). Averaged rmse between calibrated TMI (7–channel) and PR estimates (dashed); database inherent retrieval ambiguity (solid) (b).*